Spectrometry of pulsed photon radiation

IOP Publishing J. Radiol. Prot. 42 (2022) 011507 https://doi.org/10.1088/1361-6498/ac3dd0

Journal of Radiological Protection

OPEN ACCESS

RECEIVED
24 September 2021

REVISED
20 November 2021

ACCEPTED FOR PUBLICATION
26 November 2021

PUBLISHED
17 January 2022

PAPER

Spectrometry of pulsed photon radiation

Rolf Behrens*, Hayo Zutz and Julian Busse

Physikalisch-Technische Bundesanstalt (PTB), Bundesallee 100, D-38116 Braunschweig, Germany
* Author to whom any correspondence should be addressed.

E-mail: Rolf.Behrens@PTB.de

Keywords: spectrometry, pulsed photon radiation, Bayesian analysis, uncertainty, coverage interval

Abstract

The energy distribution (spectrum) of pulsed photon radiation can hardly be measured using active devices, therefore, a thermoluminescence detector (TLD)-based few-channel spectrometer is used in combination with a Bayesian data analysis to help resolve this problem. The spectrometer consists of 30 TLD layers interspaced by absorbers made of plastics and metals with increasing atomic numbers and thickness. Thus, the main idea behind the device is the deeper the radiation penetrates—the higher the radiation's energy when the radiation impinges perpendicular to the front of the spectrometer. From the doses measured in the TLD layers and from further prior available information, the photon spectrum is deduced using a Bayesian data analysis leading to absolute spectra and doses including their uncertainties and coverage intervals. This spectrometer was successfully used in two different scenarios, i.e. for the spectrometry of the radiation field two different industrial type open beam pulsed x-ray generators and secondly in three different radiation fields of a medical accelerator.

1. Introduction

Pulsed photon radiation is more and more present, in the low energy range up to a few hundred keV, e.g. as side effect at ultra-short, pulsed laser machines used for materials processing [1], in medical diagnostics [2], or from small, pulsed x-ray tubes for material testing such as welded seams [3], but also in the MeV range, e.g. at linear accelerators in tumor therapy [4]; even extreme laser driven radiation is investigated [5]. Depending on the pulse duration, pulse structure (single or repeated, regular or not), dose and dose rate per pulse, neither spectrometers nor dosemeters function reliably [6]—e.g. due to pile-up or dead time effects. Therefore, in this work, a spectrometer based on the passive detection method of thermoluminescence dosimetry is used [7, 8]. From its readings both the spectra as well as the total dose in radiation fields as described above are measured and analyzed—with the whole process of measurement and data evaluation being validated in well-known radiation fields beforehand. The spectrometer has recently been used in the low photon energy range, i.e. up to about 30 keV [9], while it is applied in the medium (up to a few hundred keV) to high energy range (up to a few MeV), in this work.

2. Measurements and data evaluation

2.1. Measurements

For the measurements a thermoluminescence detector (TLD)-based few-channel spectrometer (FCS) was used. In this spectrometer, TLD700 detectors, i.e. TLDs made of ^{7}LiF, were used interspaced by ten filters made of polymethyl methacrylate and 20 filters made of metals with increasing atomic number (from 13 up to 74) and increasing thickness (from 0.1 up to 19 mm) (see figure 1) [7, 8]. The penetration depth of the x-ray radiation in the spectrometer depends on the energy resulting in the different TLD layers in increasing doses per incident fluence (responses) with increasing photon energy but decreasing doses from the front to the back. By this, the energy-resolved and absolute spectrum of the radiation, including the uncertainties and coverage intervals of the spectrum as well as their characteristics such as mean energy, $\bar{E}$, air kerma, K_a, operational dose quantities like personal dose equivalent at 10 mm depth, H_p (10), and others and the

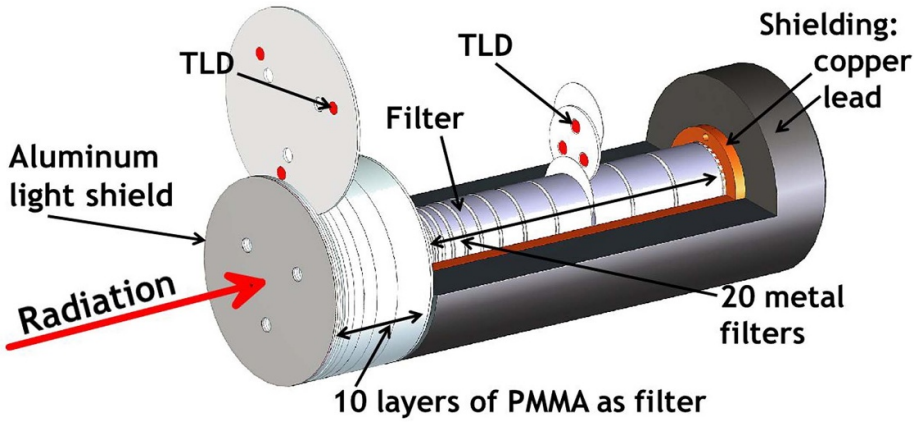

Figure 1. Sketch of the TLD-based spectrometer. Basic principle: the deeper the radiation penetrates, the higher its energy.

corresponding conversion coefficients from air kerma to the operational quantities, h, can be determined from the dose values in the TLD layers by means of Bayesian spectrum deconvolution (i.e. by mathematical methods).

TLDs, as passive detectors, are unaffected by the time structure of the radiation field, and, therefore, circumvent all difficulties electronic detectors face when used in pulsed radiation fields.

The experimental setups are shown in figure 2: firstly, two different industrial type open beam battery-powered pulsed x-ray generators from Golden Engineering, an XR200 (with 150 kV tube voltage) and an XRS4 (with 370 kV tube voltage) were placed in front of the few-channel spectrometer.

Secondly, the few-channel spectrometer was used for the spectrometry of the radiation field of a medical accelerator. For this, the spectrometer was placed at 5.5 m distance from a medical accelerator (with 25 MV accelerating voltage) with a 2 m concrete shielding wall in-between at two different beam cross sections, see below. This corresponds to the situation of non-optimal shielding in the vicinity of such an accelerator where medical or operating staff could be located. Therefore, this scenario is to be considered for use in future as a reference field for testing active personal or area dosemeters.

Furthermore, in another experiment, two more few-channel spectrometer were placed at the reference position of the radiation field, i.e. at 1 m distance from the accelerator head (isocenter of the accelerator, see figure 2). The radiation fields at the latter position are well known. Therefore, these two latter spectrometers as well as two more placed in the radiation fields of well-known x-ray tubes were used for the purpose of validation of the measurements in the unknown fields and its data evaluation. Details regarding the data evaluation follow in the section 2.2 while details regarding the validation follow in section 3.

At the medical accelerator, the maximum accelerating voltage was 25 MV possibly resulting in photoneutrons producing a significant dose reading in the TLDs. Especially thermal neutrons but also those with larger energies can produce significant readings in the TLDs leading to wrong results as all dose values were assumed to origin from photons. Therefore, the possible neutron influence on the TLDs was investigated for the two types of experiment at the 25 MV accelerator, i.e. at the isocenter for the purpose of validation as well as behind the shielding wall.

(a) For the irradiations at the isocenter of the accelerator (for validation purposes), as a first guess, the corresponding dose readings in the TLDs were assumed to origin from photons only. This assumption turned out to be correct for two reasons: firstly, the TLDs used were TLD700 material assuming a maximum of about 0.01 % ^{6}LiF compared to more than 95 % ^{7}LiF in the detectors [10] resulting in a very low sensitivity to thermal neutrons; secondly, the corresponding spectra obtained via the data evaluation described below in section 2.2 agree quite well with the correct spectra, even at 25 MV accelerating voltage, see section 3 and figure 3 in it.

(b) Behind the shielding wall, significantly more thermal neutrons could be present due to the moderation process in the 2 m concrete wall. Therefore, the neutron contamination was estimated using measurements with Physikalisch-Technische Bundesanstalts (PTB's) Bonner Sphere spectrometer [11]. From a neutron spectrum with two dominant contributions, one at thermal energy (around 25 meV) and one slightly below 1 MeV, the resulting dose reading in the TLDs in the few-channel spectrometer was estimated by multiplication with the corresponding kerma factors for ^{6}Li (for the neutron fluence around 25 meV multiplied by 0.01 % due to the small amount of ^{6}Li in the TLDs) and ^{7}Li (for the neutron

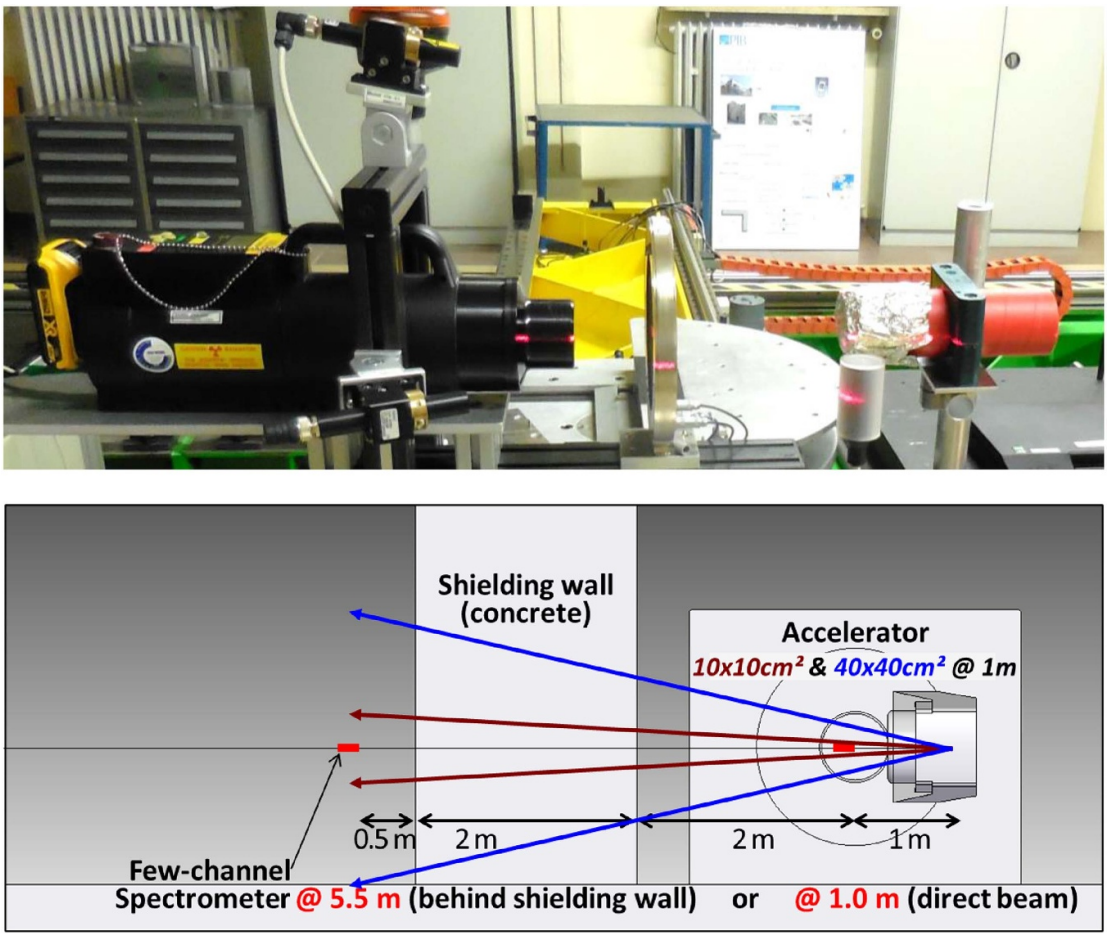

Figure 2. Experimental setups. Top: an industrial type open beam x-ray generator, XRS4, left, and a few-channel spectrometer, red (right). Bottom: sketch of the medical accelerator, right, a 2 m concrete shielding wall, middle, and the two alternative positions of the few-channel spectrometer, red (small rectangles).

fluence around 1 MeV) [12]. From this, the maximum possible dose reading due to neutrons resulted to be in the order of 0.1 μGy and below during the irradiation times of the two few-channel spectrometer [13]. The minimum dose values in the TLDs used for the data evaluation were approximately 50 μGy. Thus, a significant contribution due to neutrons could be excluded.

2.2. Data evaluation

A Bayesian data evaluation was performed using the WinBUGS software [14] which, besides the photon spectrum, also supplies the corresponding uncertainties and coverage intervals. The following prior information for the photon spectra was included in the data evaluation: (a) a smooth rise with increasing energy; (b) an exponential decrease at higher energies (due to the typical spectral shape of Bremsstrahlung spectra); (c) a peak in the spectrum at the energy of the expected characteristic fluorescence radiation (if any, like for the measurement at x-ray tubes according its anode material). The method of analysis is outlined in detail in appendix A.

3. Validation of the data evaluation

To ensure that the evaluation method is reliable, the spectrometer was irradiated in four known reference radiation fields of PTB at different photon energies, i.e. at an x-ray facility usually used for calibrating and type testing radiation protection dosemeters and secondary ionization chambers as well at a medical accelerator usually used for calibrating secondary ionization chambers as used in clinicals. Figure 3 shows the spectra from the corresponding data evaluations compared to the spectra assumed to be correct. The correct ones were determined for x-ray spectra using a high-purity germanium spectrometer [15, 16] and for spectra from a medical accelerator by an optimization process using calculated spectra and measured depth dose curves [8]. The fluence spectra were converted to air kerma, K_a, and dose equivalent, H, using the

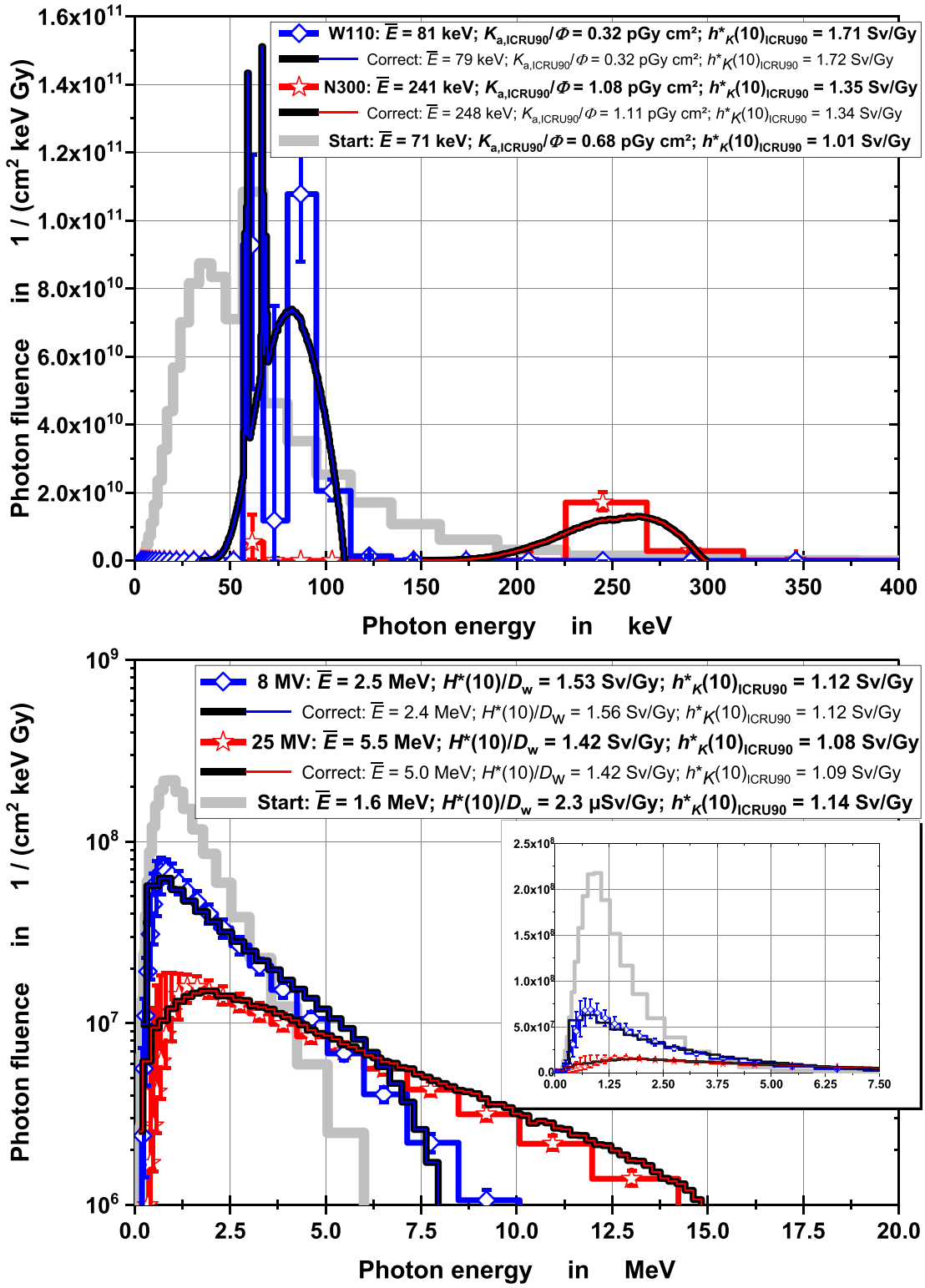

Figure 3. Validation in reference radiation fields at PTB: absolute comparison of the spectra measured with the few-channel spectrometer (blue and red line with symbols) and the correct ones, black lines. Start describes the *a priori* information used for the data evaluation. Top: spectra from conventional x-ray tubes at different high voltages according to ISO 4037-1 [21] (fluence per 1 Gy air kerma) and bottom: spectra from a medical accelerator at different accelerating voltages (fluence per 1 Gy absorbed dose to water). The bottom graph has a logarithmic ordinate and an insert with a linear one and a smaller energy range. The main characteristics of the spectra are given in the legends. The uncertainty bars show the 95 % coverage intervals ($k = 2$). All dosimetric data presented are in accordance with ICRU 90 [20], see appendix B.

corresponding conversion coefficients from air kerma to the operational quantities for mono-energetic photons, h_E [17–19]. In those cases, conversion coefficients are only available up to 10 MeV photon energy, the values above this energy level were extrapolated. The corresponding results are given in the figure's legend.

To note: the air kerma values, the conversion coefficients (from air kerma to the operational quantities such as ambient dose equivalent) as well as related correction factors stated in this work are valid for total air kerma according to ICRU 90 [20], for details see appendix B.

The 95 % coverage intervals ($k = 2$) were determined from the probability distribution for each energy channel, which is calculated as part of the Bayesian data evaluation. They incorporate the prior information on the measurements which were used for the data evaluation, i.e. the prior information described in section 2, as well as different uncertainty contributions, see appendix A.

Although the precise shape of the spectra, especially the fluorescence contribution, is not always perfectly reproduced, the absolute height of the spectra as well as their main characteristics are quite well determined using the few-channel spectrometer. Taking into account the limited spectral resolution (low number of energy bins compared to the much larger number of energy bins from the HPGe-spectrometry), this demonstrates the spectrometer's capability for an absolute spectrometry including dose determination at rather different tube and accelerator voltages, see figure 3 and its legend.

To give an impression of the data evaluation's capability, the spectra corresponding to the respective start values for the free parameters are also shown together with their characteristics.

4. Results

Figure 4 shows the absolute photon fluence spectra together with their 95 % coverage intervals and the main characteristics of the spectra. Top: spectra from two different industrial type x-ray generators and bottom: spectra from two shielded, pulsed high energy photon fields from a medical accelerator with two different beam cross sections as well as the spectrum measured in the direct beam. The two x-ray spectra overlap up to about 50 keV photon energy. This leads to the assumption that the exit windows (filtration) of the two x-ray tubes are rather similar (unfortunately, information on the windows is not available from the manufacturer). The legends show the main characteristics of the spectra, while tables 1 and 2 list several more dosimetric characteristics of the five radiation fields shown in figure 4, top and bottom respectively, together with their standard deviations ($k = 1$) and 95 % coverage intervals ($k = 2$). All values presented were taken directly from the data evaluation supplied by WinBUGS. Together with the dosimetric characteristics listed in tables 1 and 2, the spectrum averaged values of $k_{\mathrm{ISO2019,ICRU90}}$ and $(1 - g)$ are given; all dosimetric data presented are in accordance with ICRU 90 [20], see appendix B. As can be seen, $k_{\mathrm{ISO2019,ICRU90}}$ is the larger the smaller the photon energy. This results from the difference between unrenormalized and renormalized cross sections which is increasing with decreasing photon energy. In contrast, $(1 - g)$ is rather close to unity for the x-ray qualities while it decreases with increasing photon energy due to the increasing bremsstrahlung production in the MeV photon energy region.

It is obvious from the top part of figure 4 that the maximum tube voltages of the x-ray tubes stated by the manufacturer are reproduced quite well. As expected, the dose per pulse is significantly larger, i.e. roughly double for the XRS4 with 370 kV compared to the XR200 with 150 kV, while the conversion coefficient from air kerma, K_a, to ambient dose equivalent, $H^*(10)$, is rather similar. Likewise, the mean energy (fluence weighted) is significantly larger for the XRS4 than for the XR200. The measurement for the XR200 was previously performed in 2008 and evaluated at that time using another software [8]. Points to especially note are the air kerma, K_a, and the conversion coefficient to ambient dose equivalent, $h^*_K(10)$, differ to the values determined using WinBUGS (see table 4 in the former work [8]) in comparison to the legend of the top part of figure 4 in this work. The reason being the GRAVEL software used in 2008 led to non-zero fluences even at very small photon energies down to 3 keV. As the air kerma per fluence, K_a/F, strongly increases with decreasing energy, the air kerma determined at that time was more than 10 % larger compared to the air kerma determined now with WinBUGS. The larger value of K_a also led to the smaller value of $h^*_K(10)$ compared to the value determined now. For several reasons, the WinBUGS results from this work are considered to be much more reliable than the GRAVEL results. Firstly, the non-zero fluence at very small photon energies is not plausible as the XR200 exit window and the air between the XR200 and the few-channel spectrometer leads to a significant absorption of the low energy photons. Secondly, the spectra of the XR200 were measured using three different settings: at 27 cm distance with 2 × 99 pulses, at 27 cm distance with 10 × 20 pulses and at 82 cm distance with 2 × 99 pulses (see table 4 in the former work [8]). The results for the three settings determined at that time, using GRAVEL, deviated significantly from each other, especially the values for $h^*_K(10)$ which deviated by up to 8 %, while the results for the three settings determined in this work, using WinBUGS, deviated significantly less from each other, e.g. the values for $h^*_K(10)$ deviate from each other by less than 0.5 %. Thirdly, the results from WinBUGS are accompanied by uncertainties, this is not the case for the previous results. In the top part of figure 4 as well as in table 1, the results of the measurement using the XR200 are shown for the 27 cm distance with 2 × 99 pulses setting, while for the XRS4, the corresponding parameters were 30 cm distance with 10 × 10 pulses and 76 cm

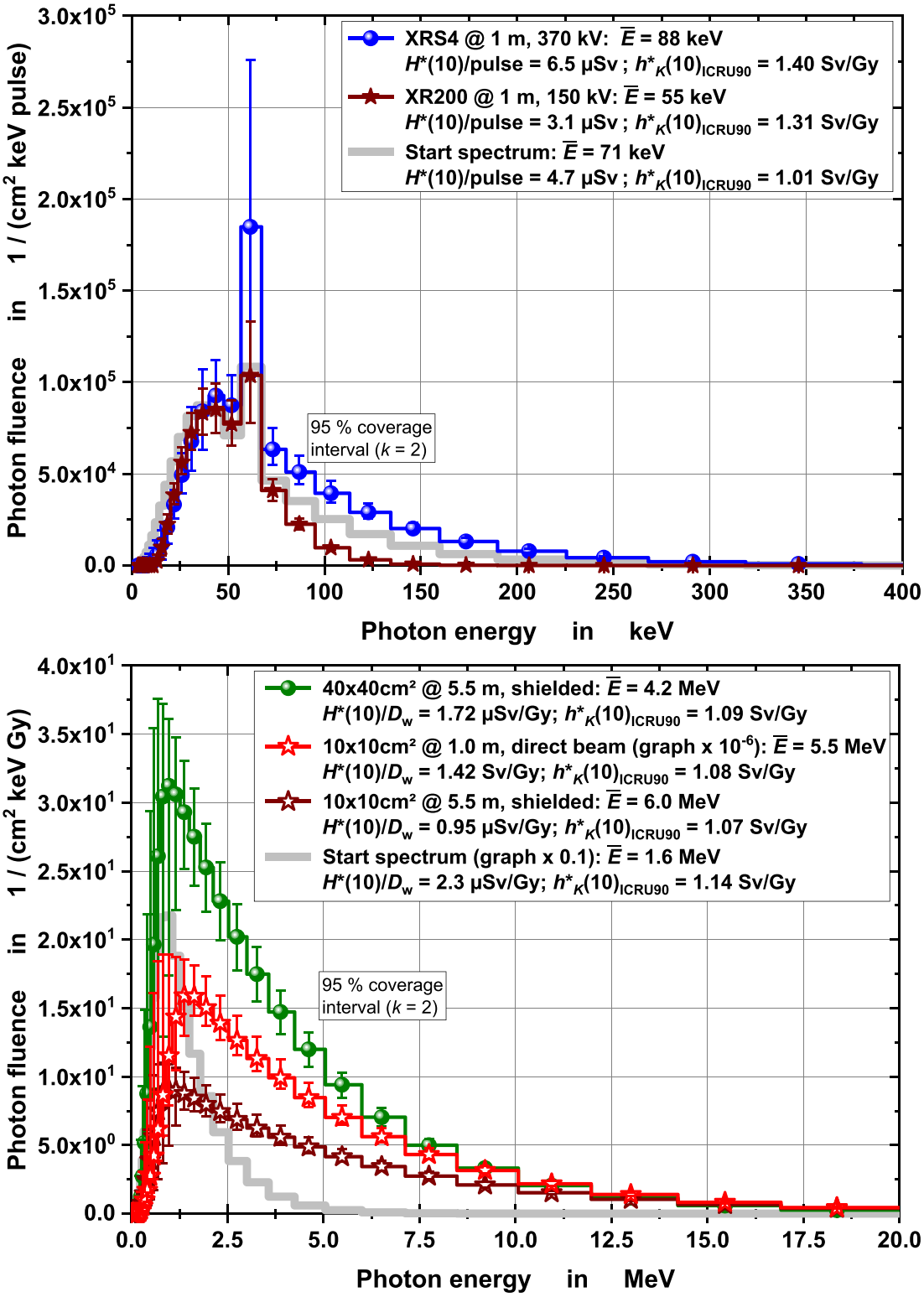

Figure 4. Photon fluence spectra together with their 95 % coverage intervals. Top: spectra from two different industrial type pulsed x-ray generators with tungsten anodes (fluence per pulse of the device) and bottom: spectra from two shielded, pulsed high energy photon fields from a medical accelerator with two different beam cross sections as well as the spectrum measured in the direct beam (fluence per 1 Gy absorbed dose to water at the reference distance of 1 m in the direct beam). The latter graph is reduced by a factor of 1×10^6, see legend. The main characteristics of the spectra are given in the legends. The uncertainty bars show the 95 % coverage intervals ($k = 2$). All dosimetric data presented are in accordance with ICRU 90 [20], see appendix B.

distance with 60 × 10 pulses of which the results of the first one are presented. All results presented are normalized to a distance of 1 m and one radiation pulse.

In the bottom part of figure 4, the shielded spectra at 5.5 m from the medical accelerator are shown for two different cross-sectional areas of 40 × 40 cm^2 and 10 × 10 cm^2 (the cross sections given are valid for

Table 1. Dosimetric characteristics of the two different industrial type x-ray generators XR200 and XRS4. The most important characteristics are printed bold. All dosimetric data presented are in accordance with ICRU 90 [20], see appendix B. For $k_{\mathrm{ISO2019,ICRU90}}$ and $(1-g)$, only the value itself is given since it does not introduce any additional uncertainty compared to the values of the quantities to which it is multiplied, see equations in appendix B.

	XR200 @ 1.0 m, 150 kV		XRS4 @ 1.0 m, 370 kV	
$K_{\mathrm{a,ICRU90}}$/pulse	(2.38 ± 0.15) µGy Gy^{-1}	[2.12; 2.69] µGy Gy^{-1}	(4.7 ± 0.3) µGy Gy^{-1}	[4.2; 5.3] µGy Gy^{-1}
$H^*(10)$/pulse	**(3.11 ± 0.18) µSv Gy^{-1}**	**[2.78; 3.50] µSv Gy^{-1}**	**(6.5 ± 0.4) µSv Gy^{-1}**	**[5.9; 7.3] µSv Gy^{-1}**
$H'(0.07)$/pulse	(3.27 ± 0.20) µSv Gy^{-1}	[2.93; 3.69] µSv Gy^{-1}	(6.6 ± 0.4) µSv Gy^{-1}	[5.9; 7.4] µSv Gy^{-1}
$\bar{E}$	**(54.6 ± 0.4) keV**	**[53.8; 55.4] keV**	**(88.0 ± 1.5) keV**	**[85.3; 91.0] keV**
$h^*_K(10)_{\mathrm{ICRU90}}$	**(1.31 ± 0.02) Sv Gy^{-1}**	**[1.26; 1.35] Sv Gy^{-1}**	**(1.40 ± 0.05) Sv Gy^{-1}**	**[1.25; 1.46] Sv Gy^{-1}**
$h_{pK}(10)_{\mathrm{ICRU90}}$	(1.38 ± 0.03) Sv Gy^{-1}	[1.32; 1.42] Sv Gy^{-1}	(1.49 ± 0.05) Sv Gy^{-1}	[1.34; 1.55] Sv Gy^{-1}
$h'_K(3)_{\mathrm{ICRU90}}$	(1.38 ± 0.02) Sv Gy^{-1}	[1.34; 1.41] Sv Gy^{-1}	(1.42 ± 0.04) Sv Gy^{-1}	[1.30; 1.46] Sv Gy^{-1}
$h_{pK}(3)_{\mathrm{cyl,ICRU90}}$	(1.37 ± 0.02) Sv Gy^{-1}	[1.33; 1.40] Sv Gy^{-1}	(1.41 ± 0.04) Sv Gy^{-1}	[1.28; 1.45] Sv Gy^{-1}
$h'_K(0.07)_{\mathrm{ICRU90}}$	(1.38 ± 0.01) Sv Gy^{-1}	[1.36; 1.40] Sv Gy^{-1}	(1.41 ± 0.02) Sv Gy^{-1}	[1.35; 1.43] Sv Gy^{-1}
$h_{pK}(0.07)_{\mathrm{rod,ICRU90}}$	(1.11 ± 0.01) Sv Gy^{-1}	[1.10; 1.11] Sv Gy^{-1}	(1.13 ± 0.01) Sv Gy^{-1}	[1.10; 1.14] Sv Gy^{-1}
$h_{pK}(0.07)_{\mathrm{slab,ICRU90}}$	(1.43 ± 0.01) Sv Gy^{-1}	[1.41; 1.45] Sv Gy^{-1}	(1.48 ± 0.02) Sv Gy^{-1}	[1.42; 1.51] Sv Gy^{-1}
$K_{\mathrm{a,ICRU90}}/F$	(0.48 ± 0.10) pGy cm^2	[0.46; 0.50] pGy cm^2	(0.51 ± 0.10) pGy cm^2	[0.48; 0.56] pGy cm^2
$k_{\mathrm{ISO2019,ICRU90}}$	**1.0185**		**1.0109**	
$(1-g)$	**0.9996**		**0.9995**	
	Value ± standard deviation ($k=1$)	Coverage interval (95 %, $k=2$)	Value ± standard deviation ($k=1$)	Coverage interval (95 %, $k=2$)

Table 2. Dosimetric characteristics of the two shielded, pulsed high energy photon fields from a medical accelerator at two different beam cross sections. For comparison, the characteristics of the direct beam with 10 × 10 cm^2 is shown on the left. The most important characteristics are printed bold. All dosimetric data presented are in accordance with ICRU 90 [20], see appendix B. For $k_{\mathrm{ISO2019,ICRU90}}$ and $(1-g)$, only the value itself is given since it does not introduce any additional uncertainty compared to the values of the quantities to which it is multiplied, see equations in appendix B.

	10 × 10 cm^2; direct beam; @ 1 m		10 × 10 cm^2; 2 m concrete; @ 5.5 m		40 × 40 cm^2; 2 m concrete; @ 5.5 m	
$K_{\mathrm{a,ICRU90}}/D_{\mathrm{w,ref}}$	(1.32 ± 0.06) Gy Gy^{-1}	[1.18; 1.41] Gy Gy^{-1}	(0.88 ± 0.04) µGy Gy^{-1}	[0.81; 0.98] µGy Gy^{-1}	(1.57 ± 0.07) µGy Gy^{-1}	[1.43; 1.72] µGy Gy^{-1}
$H'(10)/D_{\mathrm{w,ref}}$	**(1.42 ± 0.07) Sv Gy^{-1}**	**[1.32; 1.57] Sv Gy^{-1}**	**(0.95 ± 0.05) µSv Gy^{-1}**	**[0.87; 1.05] µSv Gy^{-1}**	**(1.72 ± 0.08) µSv Gy^{-1}**	**[1.56; 1.89] µSv Gy^{-1}**
$H'(0.07)/D_{\mathrm{w,ref}}$	(1.42 ± 0.07) Sv Gy^{-1}	[1.32; 1.57] Sv Gy^{-1}	(0.95 ± 0.05) µSv Gy^{-1}	[0.87; 1.05] µSv Gy^{-1}	(1.72 ± 0.08) µSv Gy^{-1}	[1.56; 1.89] µSv Gy^{-1}
$\bar{E}$	**(5.5 ± 0.2) MeV**	**[5.1; 5.7] MeV**	**(6.0 ± 0.2) MeV**	**[5.6; 6.4] MeV**	**(4.2 ± 0.1) MeV**	**[3.9; 4.5] MeV**
$h^*_K(10)_{\mathrm{ICRU90}}$	**(1.08 ± 0.01) Sv Gy^{-1}**	**[1.11; 1.12] Sv Gy^{-1}**	**(1.07 ± 0.01) Sv Gy^{-1}**	**[1.07; 1.08] Sv Gy^{-1}**	**(1.09 ± 0.01) Sv Gy^{-1}**	**[1.09; 1.10] Sv Gy^{-1}**
$h_{pK}(10)_{\mathrm{ICRU90}}$	(1.08 ± 0.01) Sv Gy^{-1}	[1.11; 1.12] Sv Gy^{-1}	(1.07 ± 0.01) Sv Gy^{-1}	[1.07; 1.08] Sv Gy^{-1}	(1.09 ± 0.01) Sv Gy^{-1}	[1.09; 1.10] Sv Gy^{-1}
$h'_K(3)_{\mathrm{ICRU90}}$	(1.08 ± 0.01) Sv Gy^{-1}	[1.11; 1.12] Sv Gy^{-1}	(1.08 ± 0.01) Sv Gy^{-1}	[1.07; 1.08] Sv Gy^{-1}	(1.09 ± 0.01) Sv Gy^{-1}	[1.09; 1.10] Sv Gy^{-1}
$h_{pK}(3)_{\mathrm{cyl,ICRU90}}$	(1.06 ± 0.01) Sv Gy^{-1}	[1.09; 1.10] Sv Gy^{-1}	(1.05 ± 0.01) Sv Gy^{-1}	[1.04; 1.05] Sv Gy^{-1}	(1.07 ± 0.01) Sv Gy^{-1}	[1.07; 1.08] Sv Gy^{-1}
$h'_K(0.07)_{\mathrm{ICRU90}}$	(1.08 ± 0.01) Sv Gy^{-1}	[1.11; 1.12] Sv Gy^{-1}	(1.07 ± 0.01) Sv Gy^{-1}	[1.07; 1.08] Sv Gy^{-1}	(1.09 ± 0.01) Sv Gy^{-1}	[1.09; 1.10] Sv Gy^{-1}
$h_{pK}(0.07)_{\mathrm{rod,ICRU90}}$	(1.07 ± 0.01) Sv Gy^{-1}	[1.10; 1.11] Sv Gy^{-1}	(1.07 ± 0.01) Sv Gy^{-1}	[1.06; 1.07] Sv Gy^{-1}	(1.08 ± 0.01) Sv Gy^{-1}	[1.08; 1.09] Sv Gy^{-1}
$h_{pK}(0.07)_{\mathrm{slab,ICRU90}}$	(1.09 ± 0.01) Sv Gy^{-1}	[1.12; 1.13] Sv Gy^{-1}	(1.08 ± 0.01) Sv Gy^{-1}	[1.08; 1.09] Sv Gy^{-1}	(1.10 ± 0.01) Sv Gy^{-1}	[1.10; 1.11] Sv Gy^{-1}
$K_{\mathrm{a,ICRU90}}/F$	(14.8 ± 0.4) pGy cm^2	[13.6; 14.9] pGy cm^2	(15.9 ± 0.5) pGy cm^2	[15.1; 16.9] pGy cm^2	(11.9 ± 0.4) pGy cm^2	[11.4; 12.8] pGy cm^2
$k_{\mathrm{ISO2019,ICRU90}}$	**0.9997**		**0.9996**		**0.9997**	
$(1-g)$	**0.9691**		**0.9640**		**0.9770**	
	Value ± standard deviation ($k=1$)	Coverage interval (95 %, $k=2$)	Value ± standard deviation ($k=1$)	Coverage interval (95 %, $k=2$)	Value ± standard deviation ($k=1$)	Coverage interval (95 %, $k=2$)

1.0 m distance from the accelerator). The beginning of the 2 m shielding wall is located at 3 m from the accelerator. Thus, the beam cross-sections of the unscattered beams are 120 × 120 cm^2 and 30 × 30 cm^2,

respectively, at the wall's 'beam entrance' and 200 × 200 cm^2 and 50 × 50 cm^2 at the wall's 'beam exit' for the two radiation fields. Apart from the beam area both irradiations are equal, i.e. an accelerating voltage of 25 MV (nominal) and the same absorbed dose to water, D_w, as if the beam area of both fields were 10 × 10 cm^2 at 1 m. Due to the beam area being 16 times larger, the 40 × 40 cm^2 field covers a much higher volume in the shielding wall, resulting in much more photon scattering. Furthermore, the mean scattering angle at this field is much larger compared to that of the 10 × 10 cm^2 field. Consequently, much more photons leave the shielding wall from the large field compared to the small one. This is obvious from figure 4 and results in an almost double ambient dose equivalent, $H^*(10)$, per absorbed dose to water, D_w. Also, due to the larger scattering contribution, the mean energy of the large field is with 4.2 MeV significantly smaller than that of the small one, which is 6.0 MeV, as the photons lose energy during the scattering process. Finally, for comparison, the bottom part also shows the spectrum measured in the direct beam at 1 m distance from the accelerator (i.e. at the reference distance in the 10 × 10 cm^2 field). Here the mean energy is slightly smaller than for the same field at 5.5 m behind the 2 m concrete shielding. This can be explained by the absorption in the shielding which is more dominant for the low energy contribution of the spectrum than for its high energy part, i.e. the spectrum is 'hardened'. Furthermore, the dose is approximately 10^6 times larger in the direct beam at 1 m compared to the shielded field at 5.5 m. This is, firstly, due to the 5.5 times smaller distance resulting in a factor of approximately 30 (due to the quadratic distance law), and secondly, due to the missing absorption in the 2 m concrete wall resulting in a factor of approximately 3 × 10^4 (approximate value for photons between 1 and 4 MeV photon energy corresponding to the spectrum's region with the maximum photon fluence, due to the exponential attenuation law in 2 m concrete). Thus, even this large range of absolute photon fluences is correctly assessed using the few-channel spectrometer.

5. Conclusions

A TLD-based few-channel spectrometer for pulsed photon radiation fields and its data evaluation method were presented in detail. Measurements were performed in well-known radiation fields for the purpose of validation and, with this, to ensure traceability of the results as well as in unknown radiation fields. Its data evaluation for the application in pure photon radiation fields was improved by using a Bayesian spectrum deconvolution which enables the spectrometer to be used for the characterization of new pulsed photon reference radiation fields. It was demonstrated that the spectrometer is able to determine the absolute photon fluence and corresponding dose values in a large energy region from the keV up to the MeV range as well as in a large fluence and dose range from the μSv up to the Sv range. Thus, the few-channel spectrometer is a device reliable for an absolute photon spectrometry even in extremely pulsed radiation fields, i.e. radiation pulses in the ns range and shorter.

Acknowledgments

The authors would like to thank Marc Stützer and Markus Schrader for their contributions to the measurements at the medical accelerator, Christian Fuhg for performing the measurements with the XRS4, Phil Brüggemann for performing the read out of the many hundreds of TLDs, George Winterbottom for checking over the manuscript and Miroslav Zboril, Marcel Reginatto and Ralf Nolte for very helpful discussions regarding the neutron contribution at the accelerator fields and for comments to the manuscript; all from PTB.

Funding

This work was supported by the Bundesamt für Strahlenschutz (BfS)—Project No. 3619S2236/FV-63014, Aufbau und Charakterisierung eines Referenzfeldes zur Sicherstellung des Strahlenschutzes an Beschleunigeranlagen in Medizin und Forschung und zur Prüfung und Kalibrierung entsprechender Messgeräte'. This project was initiated by the Bundesministeriums für Umwelt, Naturschutz und nukleare Sicherheit (BMU).

Appendix A. Details of the Bayesian spectrum deconvolution

As outlined in the introduction, the spectrometer and corresponding data evaluation method has recently been used in the low photon energy range [9]. Although the process of data evaluation is in principle the same already used at that time, the appendix of that work [9] is repeated here in order to provide the full information also in this paper. The mathematical description of the experiment and thus the basic formula

to be solved to obtain the fluence spectrum from the measured data by the following representation:

$$\vec{D}_{\mathrm{meas}} \approx \boldsymbol{R} \cdot \vec{\Phi} = \vec{D}_{\mathrm{calc}}$$

with measured doses $\vec{D}_{\mathrm{meas}} = \begin{pmatrix} D_{\mathrm{meas},1} \\ \vdots \\ D_{\mathrm{meas},N} \end{pmatrix}$, calculated responses $\boldsymbol{R} = \begin{pmatrix} R_{1,1} & \cdots & R_{1,M} \\ \vdots & \ddots & \vdots \\ R_{N,1} & \cdots & R_{N,M} \end{pmatrix}$ and fluences $\vec{\Phi} = \begin{pmatrix} \Phi_1 \\ \vdots \\ \Phi_M \end{pmatrix}$. The use of the symbol $\approx$ is meant to indicate that a strict equality is not achievable in practice due to uncertainties associated with the measurement. The spectrometer consists of $N = 30$ TLD layers. The fluence was binned into $M = 60$ energy channels (with logarithmically increasing mean energy, as the energy resolution gets worse as the energy increases, to cover the range from 3 keV to 100 MeV photon energy).

The data, D_{meas}, and the response matrix, $\boldsymbol{R}$, are known ($\boldsymbol{R}$ was calculated using the Monte Carlo radiation transport simulation package EGS4 [22–24] while the fluences, Φ, are determined from the Bayesian analysis

$$\Phi(E)_x = \begin{cases} 0 & \text{for} \quad E < E_{\mathrm{rise,start}} \\ a_{\mathrm{fluor}} \cdot \delta\left(E - E_{\mathrm{fluor}}\right) + a_{\mathrm{exp}} \cdot \exp\left(s_{\mathrm{exp}} \cdot E\right) \cdot \left\{1 + \cos\left[\left(E \cdot m_{\mathrm{rise}} + b_{\mathrm{rise}}\right) \cdot \pi\right]\right\}/2 & \text{for} \quad E_{\mathrm{rise,start}} < E < E_{\mathrm{rise,end}} \\ a_{\mathrm{fluor}} \cdot \delta\left(E - E_{\mathrm{fluor}}\right) + a_{\mathrm{exp}} \cdot \exp\left(s_{\mathrm{exp}} \cdot E\right) & \text{for} \quad E_{\mathrm{rise,end}} < E \end{cases}$$

with a_{fluor} the amplitude of the fluorescence radiation (if expected, e.g. from x-ray tubes, otherwise zero); E_{fluor} the energy of the fluorescence radiation (if expected, otherwise not in the model), a_{exp} the amplitude of the exponential decay, s_{exp} the slope of the exponential decay, $m_{\mathrm{rise}} = 1/\left(E_{\mathrm{rise,end}} - E_{\mathrm{rise,start}}\right)$, $b_{\mathrm{rise}} = -m_{\mathrm{rise}} \cdot E_{\mathrm{rise,end}}$, $E_{\mathrm{rise,start}}$ the energy where the rise of the spectrum starts, $E_{\mathrm{rise,end}}$ the energy where the spectrum turns into the exponential decay. In total, these are eight parameters of which two depend on other parameters (m_{rise} and b_{rise}). For x-ray spectra from tubes with a tungsten anode, E_{fluor} was chosen to be constant with 59 keV corresponding to the rounded energy of the K_α emission line from tungsten leading to five free parameters. In the energy range above about 600 keV maximum energy, e.g. from medical accelerators, the amplitude of the fluorescence radiation, a_{fluor}, was assumed to be zero leading to four free parameters. The free parameters were determined from the data using a program written with the Bayesian software WinBUGS [14]. Appropriate initial values and ranges within which the optimization process was allowed to vary the parameters were chosen for the evaluation carried out by WinBUGS. The methods to account for the uncertainty of the TLD's absolute calibration (3 %), the spectrometer's distance (0.25 cm up to 1 cm) depending on the experiment's geometry) and the response matrix (3 %–6 % increasing with decreasing energy) are described in the literature [25]. All uncertainties given in brackets are standard uncertainties ($k = 1$).

Appendix B. Values for air kerma, K_a, and conversion coefficients for operational quantities, h: ICRU-90 vs. ISO-4037

As already mentioned in the main text, the air kerma values, the conversion coefficients (from air kerma to the operational quantities such as ambient dose equivalent) as well as related correction factors stated in this work are total air kerma according to ICRU 90 [20], $K_{\mathrm{a,ICRU90}}$, i.e. using renormalized cross sections for the mass-energy absorption coefficients or air [20], (μ_{en}/ρ). However, the values for h_{E} for mono-energetic photons are related to the collision air kerma, $K_{\mathrm{a,col}}$, based on unrenormalized cross sections—as was the case in the outdated but still often used version of ISO4037-3 from 1999 [26] while the current version of ISO4037-3 [27] is based on the total air kerma, $K_{\mathrm{a,total}}$, see ISO4037-2 [28], but also based on unrenormalized cross sections (μ_{en}/ρ).

To obtain $K_{\mathrm{a,ISO2019}}$ and h_{ISO2019}, alternative values which are compatible with the values in ISO4037-3 [21], from the values for $K_{\mathrm{a,ICRU90}}$ and h_{ICRU90} stated in this work the following equations need to be used:

$$K_{\mathrm{a,ISO2019}} = K_{\mathrm{a,ICRU90}} \cdot k_{\mathrm{ISO2019,ICRU90}} \text{ and } h_{\mathrm{ISO2019}} = \frac{h_{\mathrm{ICRU90}}}{k_{\mathrm{ISO2019,ICRU90}}}$$

with

$$k_{\mathrm{ISO2019,ICRU90}} = \frac{K_{\mathrm{a,total}}}{K_{\mathrm{a,ICRU90}}} = \frac{\left(\frac{\mu_{\mathrm{en}}}{\varrho}\right)_{\mathrm{not\_renormalized}}}{\left(\frac{\mu_{\mathrm{en}}}{\varrho}\right)_{\mathrm{renormalized}}}$$

To obtain corresponding values which are compatible with the values in the outdated ISO4037-3 [26], the following equations need to be used:

$$K_{\mathrm{a,ISO1999}} = \{K_{\mathrm{a,ICRU90}} \cdot k_{\mathrm{ISO2019,ICRU90}} \cdot (1-g)\} \text{ and } h_{\mathrm{ISO1999}} = \frac{c_{K,\mathrm{ICRU90}}}{\{k_{\mathrm{ISO2019,ICRU90}} \cdot (1-g)\}}$$

with g being the fraction of the kinetic energy transferred to charged particles that is subsequently lost on average in radiative processes (bremsstrahlung, in-flight annihilation, and fluorescence radiations) as the charged particles slow to rest in the material (air) [20].

Thus, of course, the values for the operational quantities, H, are independent of the scheme used, be it according to ICRU90, ISO1999 or ISO2019 as the corresponding corrections cancel each other out during the multiplication leading to the operational quantity:

$$H = K_{\mathrm{a}} \cdot h.$$

ORCID iDs

Rolf Behrens https://orcid.org/0000-0002-4905-7791
Hayo Zutz https://orcid.org/0000-0002-0907-6509

References

[1] Gerhard C, Viöl W and Wieneke S 2016 *Plasma-Enhanced Laser Materials Processing. Plasma Science and Technology. Progress in Physical States and Chemical Reactions* (Tetsu Mieno, IntechOpen) (https://doi.org/10.5772/61567)
[2] Hupe O, Zutz H and Klammer J 2012 Radiation protection dosimetry in pulsed radiation fields *Presented at IRPA 13 Glasgow, Contribution TS2f.3* (available at: www.irpa.net/members/1130%20thu%20alsh%20Hupe%20TS2f.3.pdf) presentation and full paper (available at: www.irpa.net/members/TS2f.3.pdf) (Accessed 20 October 2021)
[3] Hanke R, Fuchs T and Uhlmann N 2008 X-ray based methods for non-destructive testing and material characterization *Nucl. Instrum. Methods Phys. Res.* A **59** 14
[4] Zhu T C and Wang K K H 2013 Linear accelerators (LINAC) *Encyclopedia of Radiation Oncology* ed L W Brady and T E Yaeger (Berlin: Springer) (https://doi.org/10.1007/978-3-540-85516-3_37)
[5] Labate L *et al* 2020 Toward an effective use of laser-driven very high energy electrons for radiotherapy: feasibility assessment of multi-field and intensity modulation irradiation schemes *Sci. Rep.* **10** 17307
[6] Ankerhold U, Hupe O and Ambrosi P 2009 Deficiencies of active electronic radiation protection dosemeters in pulsed fields *Radiat. Prot. Dosim.* **135** 149
[7] Behrens R and Ambrosi P 2002 A TLD-based few-channel spectrometer for mixed photon, electron, and ion fields with high fluence rates *Radiat. Prot. Dosim.* **101** 73
[8] Behrens R 2009 A spectrometer for pulsed and continuous photon radiation *J. Instrum.* **4** P03027
[9] Behrens R, Pullner B and Reginatto M 2021 Measurements at laser materials processing machines: spectrum deconvolution including uncertainties and model selection *J. Sens. Sens. Syst.* **10** 13
[10] Banaeel N, Goodarzi K and Ali Nedaie H 2021 Neutron contamination in radiotherapy processes: a review study *J. Radiat. Res.* **62** 947–54
[11] Wiegel B and Alevra A V 2002 NEMUS—the PTB neutron multisphere spectrometer *Nucl. Instrum. Methods Phys. Res.* A **476** 36–41
[12] Caswelland R S, Coyn J J and Randolph M L 1980 Kerma factors for neutron energies below 30 MeV *Radiat. Res.* **83** 217–54
[13] Zboril M and Reginatto M 2021 Both from PTB; a report with the results of the neutron measurements is in preparation *Private Communication*
[14] Lunn D J, Thomas A, Best N and Spiegelhalter D 2010 WinBUGS—a Bayesian modelling framework: concepts, structure, and extensibility *Stat. Comput.* **10** 325
[15] Ankerhold U, Berens R and Ambrosi P 1999 X-ray spectrometry of low energy photons for determining conversion coefficients from air kerma, K_a, to personal dose equivalent, $H_p(10)$, for radiation qualities of the ISO narrow spectrum series *Radiat. Prot. Dosim.* **81** 247 The spectra are available at PTB's website, R&D of department 6.3 (available at: www.ptb.de/cms/en/ptb/fachabteilungen/abt6/fb-63/information/results-of-research.html#c38395) (Accessed 3 August 2021)
[16] Ankerhold U 2000 Catalogue of x-ray spectra and their characteristic data -ISO and DIN radiation qualities, therapy and diagnostic radiation qualities, unfiltered x-ray spectra *PTB Report Dos-34* (https://doi.org/10.7795/110.20190315B)
[17] International Commission on Radiation Units and Measurements (ICRU) 1998 Conversion coefficients for use in radiological protection against external radiation *ICRU Report 57* (https://doi.org/10.1093/jicru/os29.2.Report57)
[18] Vanhavere F *et al* 2012 ORAMED: optimization of radiation protection of medical staff *EURADOS Report 2012-02* (https://doi.org/10.12768/yc01-0d55)
[19] Behrens R 2017 Conversion coefficients for $H'(3;\Omega)$ for photons *J. Radiol. Prot.* **37** 354
[20] International Commission on Radiation Units and Measurements (ICRU) 2014 Key data for ionizing-radiation dosimetry: measurement standards and applications *J. ICRU* **14** Report 90 (https://doi.org/10.1093/jicru/ndw034)
[21] International Organization for Standardization (ISO) 2019 Radiological protection—X and gamma reference radiation for calibrating dosemeters and doserate meters and for determining their response as a function of photon energy—part 1: radiation characteristics and production methods *ISO 4037-1* (available att: www.iso.org/standard/66872.html) (Accessed 3 August 2021)
[22] Nelson W R, Hirayama H and Rogers D W O 1985 The EGS4 code system *Report SLAC-265* (Stanford Linear Accelerator Center) (available at: www.slac.stanford.edu/cgi-wrap/getdoc/slac-r-265.pdf) (Accessed 3 August 2021)
[23] Namito Y, Ban S and Hirayama H 1995 LSCAT: low-energy photon-scattering expansion for the EGS4 code *National Laboratory for High Energy Physics, Japan, Report KEK Internal 95-10* (available at: http://rcwww.kek.jp/research/egs/kek/egs4/lowen.html) (Accessed 3 August 2021)

[24] Bielajew A and Rogers D W O 1987 PRESTA: the parameter reduced electron-step transport algorithm for electron Monte Carlo transport *Nucl. Instrum. Methods Phys. Res.* B **18** 165
[25] Behrens R and Reginatto M 2019 Bayesian spectrum deconvolution including uncertainties and model selection: application to x-ray emission data using WinBUGS *Radiat. Prot. Dosim.* **185** 157–67
[26] International Organization for Standardization (ISO) 1999 Radiological protection—X and gamma reference radiation for calibrating dosemeters and doserate meters and for determining their response as a function of photon energy—part 3: calibration of area and personal dosemeters and the measurement of their response as a function of energy and angle of incidence *ISO 4037-3* (available at: www.iso.org/standard/23727.html) (Accessed 3 August 2021)
[27] International Organization for Standardization (ISO) 2019 Radiological protection—X and gamma reference radiation for calibrating dosemeters and doserate meters and for determining their response as a function of photon energy—part 3: calibration of area and personal dosemeters and the measurement of their response as a function of energy and angle of incidence *ISO 4037-3* (available at: www.iso.org/standard/66874.html) (Accessed 3 August 2021)
[28] International Organization for Standardization (ISO)2019Radiological protection—X and gamma reference radiation for calibrating dosemeters and doserate meters and for determining their response as a function of photon energy—part 2: dosimetry for radiation protection over the energy ranges from 8 keV to 1,3 MeV and 4 MeV to 9 MeV*ISO 4037-2* (available at: www.iso.org/standard/66873.html) (Accessed 3 August 2021)